Optimal-Permittivity Dielectric Liners for a 4.7T Transceiver Array

Atefeh Kordzadeh[1,2], Nicola De Zanche[3,4]*

1. Department of Biomedical Engineering, University of Alberta, Edmonton, Alberta, Canada
2. Department of Electrical and Computer Engineering, University of Alberta, Edmonton, Alberta, Canada
3. Department of Medical Physics, Cross Cancer Institute, Edmonton, Alberta, Canada
4. Department of Oncology, University of Alberta, Edmonton, Alberta, Canada

*Corresponding author:

Nicola De Zanche
Department of Medical Physics
Cross Cancer Institute
11560 University Avenue
Edmonton, Alberta, Canada
T6G 1Z2

Telephone: 780-989-8155
Fax: 780-432-8615
Email: dezanche@ualberta.ca

Abstract

Placing dielectric pads adjacent to the imaging region is an effective method to increase the signal locally and also increase the radio frequency magnetic field homogeneity in magnetic resonance imaging. The use of local high permittivity pads is becoming more common, and this work focuses on the effect of larger dielectric pads on the transmit/receive performance of an array (e.g., coupling, efficiency and safety) having 8 channels, used to image a cylindrical phantom at 4.7 T (200 MHz). We investigate the effects of a dielectric liner surrounding the whole volume of interest both with and without an air gap. The simulations reveal that high permittivities are not recommended because they substantially degrade the longitudinal homogeneity, resulting in hot spots of specific absorption rate at the driven end of the array. Furthermore, high permittivities lead to dielectric resonances in the liner at frequencies close to the Larmor frequency, potentially degrading the performance of the array. Indeed, simulations and measurements confirm that a compromise must be made between improvements in field homogeneity and transmit performance, and that an optimal permittivity exists which is much lower than those commonly used in the literature. The optimal permittivity achieves minimal coupling (<–23 dB) between array elements, exhibits an intrinsic electromagnetic impedance equal to the geometric mean of those of the coil former and phantom and can be realized with inexpensive materials. For this permittivity the performance with an air gap of thickness equal to that of the liner is equivalent to that without the air gap.

1. Introduction

High static magnetic field MRI promises high signal-to-noise ratio (SNR) but is limited by radio frequency (RF) magnetic field (B_1) inhomogeneity in the sample due to short wavelength relative to the sample dimensions. These inhomogeneities in B_1 field degrade image quality and lead to bright and dark areas in the image [1]. To mitigate these effects, array excitation with control over the phase and amplitude of each element has been developed [2]. Blocks or flexible bags filled with dielectric material placed strategically near the region of interest (ROI) have also been shown to improve B_1 field homogeneity [3]. These dielectric "pads" have been increasingly used as a tool to focus the B_1 field locally and hence increase efficiency or SNR locally [4], [5].

Early dielectric pads were designed to have approximately the same dielectric constant as nearby tissues (e.g., gelatin-honey gels) to prevent electromagnetic field reflections at the dielectric boundary [6]. More recently, high-permittivity materials have been developed by mixing powdered ceramics such as barium or calcium titanate ($BaTiO_3$ and $CaTiO_3$) with deuterium oxide (D_2O) or deionized water, resulting in a suspension or slurry that is then sealed in plastic bags [7], [8], [9]. Suspensions of such materials present challenges such as the risk of leaking potentially toxic or irritating materials to the patient. Moreover the suspension can easily settle or deform, thus changing the dielectric constant and thickness of the pad [10], while the resulting large regions of liquid water give undesired visible signals. High-permittivity ceramics and D_2O are expensive materials which add dramatically to the cost of the pads, therefore the use of lower permittivities is economically advantageous.

Despite these challenges, high dielectric constant (HDC) pads with relative permittivity $\varepsilon_r > 100$ have become popular [3], [4], [7], [9]. Reference [7] shows that significant increases (20% and greater) in SNR and reduction in input power are achieved by HDC pads placed locally. Specific

absorption rate (SAR) has also been investigated [7], [11], [12], [13]. In some cases [7], [13], by introducing local HDC pads, SAR decreases as a result of a reduction in input power to generate the same amount of B_1 field. References [4], [14], and [15] predict that for every application there exists an optimal permittivity that provides the best performance. In this work we show that the optimum can be achieved with lower permittivities than those commonly reported in the literature. While most authors use local pads to focus the magnetic field locally, this work explores the effect of dielectric materials placed surrounding, and in contact with, the whole imaging volume. Recent simulations have shown that a helmet-shaped HDC shell can focus the fields of a standard body transmit coil mostly to the head, thus limiting SAR in the rest of the body [16]. The optimal permittivity was found to be very high ($\varepsilon_r = 600$). In the present work we determine, by simulation and measurement, the optimal permittivity of a dielectric liner used in conjunction with an array for imaging a cylindrical phantom at 4.7 T (200 MHz). Our arrangement is similar to that reported in [17]; there, however, the dielectric is located between the RF shield and coil conductors, which are separated from the imaging volume by an air gap. The transmit and receive performance of the array are evaluated based on standard parameters such as coil efficiency, B_1 field, and SAR. Additionally, we investigate the effect of the dielectric liner on coupling between elements, which is an important indicator of array performance that should be minimized.

2. Methods

The geometry of the coil array and the liner investigated in this work is shown in Figure 1(a). The imaging volume (phantom) is the inner cylinder in Figure 1(b), and is surrounded by an annular region of low-loss dielectric (the liner) whose purpose is to create additional displacement currents that enhance the RF B_1 field and thus SNR [4], [5]. The array's conductors are located on a 5-mm-thick acrylic (PMMA) former surrounding the liner. Consequently, four regions of dielectric media

4

are present, beginning with the outermost air region. The second is the PMMA former followed by the low-loss dielectric annulus, and lastly the lossy phantom.

<Figure 1>

When an electromagnetic field impinges on the boundary between two dielectric materials, it will experience some reflection due to the difference in the intrinsic impedance, $\eta = \sqrt{\mu/\varepsilon}$, of the two media, where ε and μ are, respectively, the dielectric constant (or permittivity) and permeability of the material [18]. Therefore the electromagnetic fields encounter primarily two dielectric boundaries where they will experience some reflection and transmission due to mismatches in the impedances of the media. The dielectric constant of the annulus determines not only the magnitude of its displacement currents, but also the reflection experienced by the fields and thus their penetration into the imaging region (phantom). Because transmission and reflection happen in the near-field region, the reflection at the boundaries does not follow the simple equations that apply in the far field. Nevertheless, the field reflections are caused by mismatches between the impedances of the two media. While insertion of the dielectric liner can degrade coil matching by introducing a reflection boundary between the coil and the phantom, if the permittivity is designed to match these two layers, S_{11} can actually be reduced, meaning that more power can enter the phantom.

Coupling due to mutual impedances between array elements is an additional quantity that affects performance [19]. Mutual impedance, $Z_{12} = R_{12} + iX_{12}$, is responsible for signal and noise transfer between coupled elements. Using reaction theory, mutual impedance can be expressed as a function of the electromagnetic fields generated when coils are excited [19], [20]:

$$Z_{ij} = \frac{-1}{I_i I_j}\left\{\iiint_{phantom+pad} E^j(r).J_p^i(r)dv + \iiint_{coil} E^j(r).J_c^i(r)dv\right\} \tag{1}$$

$$= \frac{-1}{I_i I_j} \left\{ \iiint_{phantom} (\sigma_p + j\omega\varepsilon)\, E^j(r).E^i(r)dv + \iiint_{pad} j\omega\varepsilon\, E^j(r).E^i(r)dv \right.$$

$$\left. + \iiint_{coil} E^j(r).J_c^i(r)dv \right\}.$$

Here $E^j(r)$ is the electric field generated by the current, I_j, on coil j. The term $J_c^i(r)$ refers to the current density on coil i and term $J_p^i(r)$ is the current (conduction and displacement) induced in the phantom and HDC pads by the fields of coil i.

In equation (3), the volume integral over the pad shows that its effect on the mutual impedance is proportional to its dielectric constant. The effect is especially significant for mutual resistance (see Fig. 2 of [21]) which is often negligible compared to the imaginary component when low dielectric constant pads ($\varepsilon_r \ll 100$) or air fills the gap between coil and phantom. When HDC pads are used both components of the mutual impedance are important, and the overall increase in mutual impedance creates challenges in coil array decoupling because both terms must be removed to avoid signal, power and noise transfer between channels.

The final parameter that is important in investigating the dielectric liner's performance is its resonant frequency. The dielectric liner will behave as a dielectric resonator which has a fundamental resonance frequency as well as additional modes at higher frequencies. Dielectric resonance has been exploited for MR detection [22], but in general the presence of these modes is not necessarily a benefit when a dielectric liner is added to an existing coil array that is designed to work also without the dielectric. We suggest that the resonant frequency of the dielectric liner should be far enough away from the resonant frequency of the coil array (in this case 200 MHz) to prevent an interference of this mode with the array and consequent performance degradation.

2.1.   Array and Phantom Construction

The array (Figure 1) consists of eight rectangular loops (dimensions in Table 1) made of copper tape conductors conformed to a 200-mm-diameter acrylic (PMMA) cylinder to accommodate a small head or the extremities. Capacitances (also listed in Table 1) required to make the elements resonate at 200 MHz are distributed over 8 gaps in each coil to ensure uniform current distributions. Each element includes a tuning capacitor at the side opposite the feed, which consists of a lattice balun (integrated balun and matching circuit). An RG223 coaxial cable 150 cm in length is connected to each feed circuit and all 8 cables are connected to a single grounding point consisting of an aluminum plate populated with BNC bulkhead connectors.

<Table 1>

The imaging phantom consists of a cylinder 150 mm in diameter and 180 mm in length filled with a lossy solution (3.6 g/L NaCl, 1.96 g/L $CuSO_4 \cdot 5H_2O$ [23]) with relative permittivity ε_r=78 and conductivity σ=0.8 S/m to mimic the dielectric properties of tissue.

2.2.   Liner Construction

In this work we compare liners having a wide range of permittivities (Figure 2) including the case where no liner is present (air). The highest dielectric constant material, (ε_r=150, σ=0.05 S/m), is made using a barium titanate ($BaTiO_3$) powder suspension made by mixing the ceramic powder (Alfa Aesar, MA, USA) with water with volume ratio of 0.3 ($V_{BaTiO3}/V_{Water} = 3/7$) as shown in Figure 2(a). The second material is de-ionized water which has a permittivity approximately equal to that of the phantom but much lower losses (ε_r=78, σ=0.002 S/m) (Figure 2(b)). Finally, a material was made to match the phantom's intrinsic impedance to that of the PMMA former. The intrinsic impedance of a medium having relative permittivity ε_r (and permeability μ_0) is given by [18]

$$Z = \frac{Z_0}{\sqrt{\varepsilon_r}} \ , \varepsilon_r = \left(\frac{Z_0}{Z}\right)^2 ,$$

<div align="right">(2)</div>

where Z_0 is the intrinsic impedance of free space (377 Ω). This material's impedance is chosen to be equal to the geometric mean of the impedances that electromagnetic fields experience in PMMA (189 Ω) and the phantom (43.2 Ω), resulting in 90.3 Ω. The resulting relative permittivity of 17.5 and conductivity of 0.03 S/m was achieved using a suspension of alumina (Al_2O_3, Manus Abrasive Systems Inc.) and water (Figure 2(c)) with a volume ratio of 0.5 ($V_{Alumina} = V_{Water}$). All materials are inserted into heat-sealable food storage bags (layered polyethylene and polyamide film) measuring approximately 18×6×2 cm^3, a number of which can be readily packed side by side to fill the annular space between the phantom and coil holder. The fabricated coil with dielectric liner surrounding the phantom is shown in Figure 3.

<Figure 2>

<Figure 3>

2.3. Simulations

To investigate array performance, full-wave simulations of the complete structure were performed for each liner material using High Frequency Structure Simulator (HFSS V.15, Ansys, USA). The domain was bounded by a perfect cylindrical conductor with radiation boundaries at both ends to mimic the magnet bore. Each element of the array is excited by a lumped port with 1 W of incident power, resulting in fields and scattering (*S*) parameters that can be exported for further processing. Specifically, the fields can be combined in any linear combination such as quadrature excitation (equal magnitude, with phase distributed progressively around the circle) or single-channel excitation to compare to experimental data. Simulations using 1 A current sources on each element were also performed (including all capacitors) to eliminate the effects of matching. The permittivity of the liner was varied between the four values above plus $\varepsilon_r = 35$ to complete an

approximate geometric progression. Field inhomogeneities are calculated for B_1^+ and SAR as the standard deviation of the field in a specified region relative to its mean (i.e., the coefficient of variation, CoV).

2.3.1.   Generalized Scattering Parameters

The wide range of permittivities used for the liner can modify matching conditions, and thus the corresponding coupling, considerably. To eliminate these differences in coupling due to matching, the *S* matrices are modified by introducing matching circuits adjusted so that the matching in each case is the same ($S_{ii} \approx 0$). Firstly, the *S* matrix is pre- and post-multiplied by a diagonal matrix of phase offsets (i.e., a shift in reference planes [18, p.184]) which accounts for the phase component of each matching circuit. Then the formalism of generalized *S* parameters is used to calculate a new S matrix having minimal values of $|S_{ii}|$ for an appropriate choice of new reference impedances (which is equivalent to matching by means of ideal transformers) [24]. The phase offsets and reference impedances are found by numerical optimization.

2.3.2.   Dielectric Resonance

The liner is an annular cylinder of dielectric material and thus can behave as a dielectric resonator. A dielectric resonance at the Larmor frequency will introduce potential safety issues similarly to the coupling between a traditional resonator, such as a small surface coil, placed within a volume coil. The resonant mode of the dielectric liner could also degrade the performance of the coil array by contributing little to signal sensitivity (i.e., if the B_1 field is oriented primarily along *z*) while dissipating power. Therefore the resonant frequency of the fundamental dielectric resonance mode of each liner was found by performing an eigenmode simulation for each isolated liner within radiating boundaries.

2.3.3.   Effects of an Air Gap

In practical in-vivo imaging there is typically an air gap between the coil(s) and the body for comfort or to allow air flow for cooling, breathing, etc. The effect of an air gap between the matched liner (ε_r = 17.5) and phantom is therefore investigated by reducing the thickness of the liner and forming an air gap of equal thickness. Simulations as described above are repeated for this new geometry.

2.4.   Bench Measurements

Scattering parameters of the array are measured using an Agilent 4395A vector network analyzer with an 85046 S-parameter test set (Figure 3). The 8 cables are kept as straight and parallel as possible using foam spacers and connected to the grounding plate as described above. The unused channels are terminated with 50 Ω loads.

2.5.   Imaging Measurements

The simulation results were verified by acquiring images on a 4.7 T whole-body system with a 4-channel Unity Inova console (Varian, Palo Alto, CA). Single-channel flip angle maps were acquired with one channel transmitting and receiving, while three other nearby channels were receiving the signal (Figure 4). The unused four channels were terminated with 50 Ω loads. The B_1^+ field distribution with the four liners was measured with the gradient-echo double-angle technique [25] using a 5 ms Gaussian excitation pulse and nominal flip angles of 45° and 90° (calibrated in a voxel just below the transmitting coil). In this method the ratio of the intensity of the signal at 90° over double the ratio of the signal at 45° are calculated and then converted to a flip angle map ($\alpha(x) = arccos\, I_2(x)/2I_1(x)$) [25]. The acquisition parameters for these multi-slice scans are: echo time TE=7 ms, pulse repetition time TR=1000 ms, 9 slices, FOV of 192 × 192 × 180 mm^3 and resolution of 1 × 1 × 8 mm^3. For each liner the transmit power was adjusted

to achieve the same nominal flip angle in an ROI near the transmitting coil. The transmitter gain settings were recorded and compared for each liner permittivity.

<Figure 4>

3. Results and Discussion

3.1. Simulations

An important motivation for using high permittivity liners is to increase RF magnetic field homogeneity. The B_1^+ field from the simulations (1A quadrature excitation) shows that homogeneity in the central transverse plane (Figure 5 and Table 2[1]) improves by increasing the permittivity of the liner due to the effects of local displacement currents. There is only a minor difference between liners with ε_r=78 and ε_r=150, which supports the conclusion that high permittivities are not needed. Conversely, considering the whole volume (sagittal slices in Figure 5 and Figure 6, as well as Table 2) we observe that, especially when high permittivity liners are used, longitudinal homogeneity is significantly degraded, and a B_1^+ field node appears at the end of the cylinder opposite to the driven ports.

<Figure 5>

<Figure 6>

<Table 2>

Figure 6 shows the SAR pattern plotted over the central transverse slice and a sagittal slice of the phantom, where the longitudinal asymmetry between the two ends of the phantom is clearly visible, with one or more SAR hot spots appearing at the driven end of the array. The increased SAR inhomogeneity with high permittivities is also observed in the corresponding rows of Table

---

[1] The inhomogeneity is defined in Table 2 as the standard deviation of the B_1^+ field relative to its mean.

2. Indeed, Poynting vector plots (not shown) demonstrate that high-permittivity liners couple strongly with the electric fields at the feed points, driving power preferentially to the top of the phantom rather than more uniformly along its length.

Excitation and safety excitation efficiency are defined as $E_v = B_1^+/\sqrt{P_v}$ and $S_v = B_1^+/\sqrt{\max(SAR_{10g})}$, respectively [26], where P_v is the power deposited in the volume of interest (VOI), and SAR_{10g} is the 10-gram average SAR. Because of the SAR concentrations at the driven end of the coil, high-permittivity liners degrade both transmit efficiencies by at least 15% . However, changes in efficiency using the optimal permittivity liner are insignificant. These simulations demonstrate that liners made with high permittivity materials typically found in the literature can lead to undesirable concentrations of electric fields and SAR, thus reducing efficiencies compared to those achieved with lower permittivities.

The S matrices shown in Figure 7 were obtained from those calculated by the simulations by removing differences in S_{ii} as described in Generalized Scattering Parameters. The matrices highlight the differences in coupling observed with different liner permittivities, i.e., that the optimal permittivity liner (Figure 7b) maintains mutual coupling below 0.07 (–23 dB) between all pairs of coils, while other permittivities (including air) lead to substantially higher coupling. This finding is in sharp contrast to that of Ref [15] in which no changes in noise correlation (which does depend on coil coupling, but not exclusively) [27], [28] were found.

<Figure 7>

Table 2 also lists the fundamental frequency of each liner as a dielectric resonator, corresponding to the TE$_{01\delta}$ mode in which the B$_1$ field is oriented mostly along the axis [22]. As expected, the higher the permittivity, the lower is the resonant frequency, which in the case of ε_r=150 is indeed close to 200 MHz while with lower permittivities it is far from the coil's resonant frequency and

thus more appropriate to use. Note that for a larger array built for the adult head, or tuned to 7 T, a high-permittivity liner may have multiple dielectric resonance modes near the operating frequency.

Single-element field maps (1 W port excitation) are shown in Figure 9 (top row). As observed for the quadrature fields (Table 2), high-permittivity liners degrade the penetration of fields deep inside the VOI, while nearer to the transmitting element the effect on the field intensities is minimal. High-permittivity liners also appear to excite elements on the side opposite the driven element more effectively, which is consistent with the findings above on coupling (Figure 7).

The effect of an air gap between phantom and liner on the transmit performance of the array, also investigated by simulations, reveals that matching and coupling are not changed significantly by the introduction of the gap. Fields and efficiencies compared in Table 3 indicate that the transmit and safety efficiencies are insensitive to the presence of the air gap, while the field homogeneity over the volume improves with the air gap. Consequently, the effects of the dielectric liner are also present in a more realistic situation in which air gaps are required for comfort or to allow air flow.

<Table 3>

3.2.   Bench measurements

Figure 8 shows the measured (a) and simulated (b) return loss ($|S_{11}|$) for each liner over the frequency range between 170 and 230 MHz. Besides some frequency splitting due to coupling the optimal permittivity liner improves matching as predicted by the simulations.

<Figure 8>

3.3.   Imaging Measurements

The flip angle maps acquired when one channel is transmitting (Figure 9, bottom row) show that, consistently with the simulations, the optimal permittivity liner results in the smallest overall

excitation of other elements. The remaining features of Figure 9 show broad agreement between simulations and measurements, with differences likely arising from the omission of some practical details from the simulation to avoid introducing excessive computational burden. Specifically, the simulation ignores coupling due to cables and ground connections as well as the effects of matching circuits.

<Figure 9>

The relative transmitter gains obtained during flip angle calibration are compared for each liner to their equivalents from the simulation in Table 4. We note excellent agreement and a progressively degraded sensitivity with liner permittivities above $\varepsilon_r = 1$ (also seen in Table 2). These findings are in contrast with those typically reported in the literature (e.g., [4], [5], [15]), where sensitivity usually improves with the presence of a local high-permittivity pad.

<Table 4>

4. Conclusion

This work investigates the effects of an annular dielectric liner between an array and phantom in terms of electromagnetic fields and sensitivities. The values of relative permittivities used for the liner range between 1 and 150. It was found that high permittivities ($\varepsilon_r > 100$) used in the literature give rise to liners with resonant frequencies that are close to the Larmor frequency. We recommend that the effect of dielectric resonance modes should be investigated in detail when large volumes of dielectric are present [3]. Unlike local dielectric pads, liners also introduce inhomogeneities and SAR concentrations in the longitudinal direction. Consequently, a compromise should be made between desired improvements in magnetic field homogeneity in the transverse plane and unwanted degradations in longitudinal homogeneity as well as in transmit efficiency. The optimal permittivity was found by minimizing reflections at the interfaces of the various dielectric media

14

(coil former, liner, and phantom), i.e., by choosing an intermediate intrinsic impedance equal to the geometric mean of those of the former and phantom. The materials used to achieve this permittivity are inexpensive. The optimal permittivity also minimizes coupling between elements while keeping the liner's dielectric resonance frequency at least one octave away from the Larmor frequency (Table 2). A more realistic imaging setup was also studied by adding an air gap of thickness equal to that of the liner. The array's transmit performance with the air gap is equivalent to that without the gap, while achieving better field homogeneity. These results are based on a simple geometry and therefore future work should include the study of more anatomically-accurate models. Ergonomic and practical considerations such as air gaps of uneven thickness should also be studied.

In conclusion, we have shown that the optimal permittivity of a dielectrically-lined array is much lower than those typically used in the literature. Possible explanations could be found in the encircling shape and large total volume of the dielectric annulus used here. We expect that similar results will be found in analogous cases where the volume of the dielectric is comparable to that of the imaging region.

Acknowledgements

References

[1] Robitaille P-M, Berliner L. Ultra High Field Magnetic Resonance Imaging. vol. 26. Boston, MA: Springer US; 2006.

[2] Yazdanbakhsh P, Solbach K. Active Phased Array Techniques for High-Field MRI. 3rd Eur. Conf. Antennas Propagation, Berlin, 2009, p. 1367–71.

[3] Haines K, Smith NB, Webb AG. New high dielectric constant materials for tailoring the B_1^+ distribution at high magnetic fields. J Magn Reson 2010;203:323–7.

[4] Webb AG. Dielectric Materials in Magnetic Resonance. Concepts inMagnetic Reson Part A 2011;38A(4):148–84.

[5] Luo W, Lanagan MT, Sica CT, Ryu Y, Oh S, Ketterman M, et al. Permittivity and performance of dielectric pads with sintered ceramic beads in MRI: early experiments and simulations at 3 T. Magn Reson Med 2013;70:269–75.

[6] Sunaga T, Ikehira H, Furukawa S, Tamura M, Yoshitome E, Obata T, et al. Development of a dielectric equivalent gel for better impedance matching for human skin. Bioelectromagnetics 2003;24:214–7.

[7] Yang QX, Rupprecht S, Luo W, Sica C, Herse Z, Wang J, et al. Radiofrequency field enhancement with high dielectric constant (HDC) pads in a receive array coil at 3.0T. J Magn Reson Imaging 2013;38:435–40.

[8] de Heer P, Brink WM, Kooij BJ, Webb a G. Increasing signal homogeneity and image quality in abdominal imaging at 3 T with very high permittivity materials. Magn Reson Med 2012;68:1317–24.

[9] Brink WM, Webb AG. High permittivity pads reduce specific absorption rate, improve B 1 homogeneity, and increase contrast-to-noise ratio for functional cardiac MRI at 3 T. Magn Reson Med 2014;71:1632–40.

[10] Teeuwisse WM, Brink WM, Haines KN, Webb a G. Simulations of high permittivity materials for 7 T neuroimaging and evaluation of a new barium titanate-based dielectric. Magn Reson Med 2012;67:912–8.

[11] Rennings A, Wang K, Chen L, Wetterling F, Erni D. An Electromagnetic-Simulation based Investigation of the Dielectric padding approach for head imaging at 7T. Proc. Intl. Soc. Mag. Reson. Med. 22, vol. 10, 2014, p. 3–7.

[12] Yang QX, Herse ZG, Ketterman M, Wang J, Sica C, Collins C, et al. Enhancement of RF field by high dielectric constant pad at 3T : Cervical Spine Imaging. Proc. Intl. Soc. Mag. Reson. Med., vol. 203, 2011, p. 2771.

[13] Yang QX, Wang J, Wang J, Collins CM, Wang C, Smith MB. Reducing SAR and enhancing cerebral signal-to-noise ratio with high permittivity padding at 3 T. Magn Reson Med 2011;65:358–62.

[14] Teeuwisse WM, Brink WM, Haines KN, Webb AG. Simulations of high permittivity materials for 7 T neuroimaging and evaluation of a new barium titanate-based dielectric.

Magn Reson Med 2012;67:912–8.

[15]   Teeuwisse WM, Brink WM, Webb AG. Quantitative assessment of the effects of high-permittivity pads in 7 Tesla MRI of the brain. Magn Reson Med 2012;67:1285–93.

[16]   Yu Z, Xin X, Collins CM. Potential for high-permittivity materials to reduce local SAR at a pacemaker lead tip during MRI of the head with a body transmit coil at 3 T. Magn Reson Med 2017;78:383–6.

[17]   Foo TKF, Hayes CE, Kang Y-W. Reduction of RF penetration effects in high field imaging. Magn Reson Med 1992;23:287–301.

[18]   Pozar DM. Microwave Engineering. Third Edit. John Wiley & Sons, Inc.; 2005.

[19]   Wright SM, Wald LL. Theory and application of array coils in MR spectroscopy. NMR Biomed 1997;10:394–410.

[20]   Harrington RF. Time-harmonic electromagnetic fields. IEEE Press : Wiley-Interscience; 2001.

[21]   Kordzadeh A, De Zanche N. Control of Mutual Coupling in High-Field MRI Transmit Arrays in the Presence of High-Permittivity Liners. IEEE Trans Microw Theory Tech 2017:1–7.

[22]   Aussenhofer SA, Webb AG. Design and evaluation of a detunable water-based quadrature HEM 11 mode dielectric resonator as a new type of volume coil for high field MRI. Magn Reson Med 2012;68:1325–31.

[23]   Och JG, Clarke GD, Sobol WT, Rosen CW, Mun SK. Acceptance Testing of Magnetic Resonance Imaging Systems: Report of AAPM Nuclear Magnetic Resonance Task Group No. 6. Med Phys; 19 (1): 217-229.

[24]   Carlin HJ, Giordano A. B., Network Theory: An Introduction to Reciprocal and Nonreciprocal Circuits. Prentice-Hall, Inc., Englewood cliffs, N.J.; 1946.

[25]   Stollberger R, Wach P. Imaging of the active B_1 field in vivo. Magn Reson Med 1997;38:336.

[26]   Kozlov M, Turner R. Influence of Shield Distance on RF Transmit Performance for a 7T Multi-channel MRI Loop Array. Prog Electromagn Res Symp Proc 2012:255–9.

[27]   Brown R, Yi Wang. Transmission line effects on the coil noise correlation matrix in MRI. 30th Annu. Int. Conf. IEEE Eng. Med. Biol. Soc., IEEE; 2008, p. 2032–5.

[28]   Maunder A, Fallone BG, Daneshmand M, De Zanche N. Experimental verification of SNR and parallel imaging improvements using composite arrays. NMR Biomed 2015;28:141–53.

Tables

Table 1: Design parameters for the coil array.

W_{trace}(mm)	W_{coil}(mm)	L(mm)	S(mm)	C_{t1}(pF)	C_{t2}(pF)
10	69	180	10	13	15

Table 2: Transmit performance parameters of the coil array in presence of the different dielectric liners at 200 MHz (HFSS simulation, 1A quadrature excitation except for the first row which is an eigenmode solution).

	ε_r=1	ε_r =17.5	ε_r =35	ε_r =78	ε_r =150
Resonant frequency of liner (MHz)	-	549	436	292	<u>216</u>
B_1^+ standard deviation/mean (volume)	26.3%	34.4%	35.1%	38.4%	42.7%
B_1^+ standard deviation/mean (slice)	23.9%	19.7%	18.7%	18.4%	17.2%
SAR standard deviation/mean (volume)	46.2%	50.0%	60.7%	70.0%	73.7%
Max (SAR)/mean(SAR)	2.10	2.18	2.60	3.05	3.58
$B_{1,avg}^+/\sqrt{P_V}$ **(µT/√W)**	0.52	0.50	0.47	0.46	0.42
$B_{1,avg}^+/\sqrt{max(SAR_{10g})}$ **(µT/√(W/kg))**	0.68	0.65	0.55	0.49	0.43

Table 3: Summary of HFSS simulations (1A quadrature excitation) comparing fields and efficiencies for the case where no air gap is present versus adding an air gap between phantom and liner (ε_r =17.5).

	With air gap	Without air gap
$B_1{}^+$ standard deviation/mean (volume)	28.3%	34.4%
$B_1{}^+$ standard deviation/mean (slice)	23.3%	19.7%
SAR standard deviation/mean (volume)	33.7%	50.0%
$B_{1,avg}^+/\sqrt{P_V}$ (µT/√W)	0.48	0.50
$B_{1,avg}^+/\sqrt{max(SAR_{10g})}$ (µT/√(W/kg))	0.66	0.65
Max (SAR)/mean(SAR)	2.21	2.18

Table 4: Simulated and measured sensitivity ($B_1^+/\sqrt{P_v}$) to achieve a given flip angle or B_1 amplitude in an ROI directly below the driven element for each dielectric liner.

	ε_r=1	ε_r =17.5	ε_r =78	ε_r =150
Measured (1/relative TX gain)	1	0.89	0.79	0.63
Simulated relative sensitivity	1	0.92	0.79	0.77

Figure Captions

Figure 1: (a) Head coil array, and (b) dielectric media shown in a transverse slice.

Figure 2: Fabricated dielectric pads: (a) high dielectric constant pad (ε_r = 150), (b) distilled water pad, (c) matching pad (alumina, ε_r = 17.5).

Figure 3: Fabricated array with dielectric liner bags and phantom (left). Instrumentation used for bench testing (RF grounding / loading plate and network analyzer) is shown on the right.

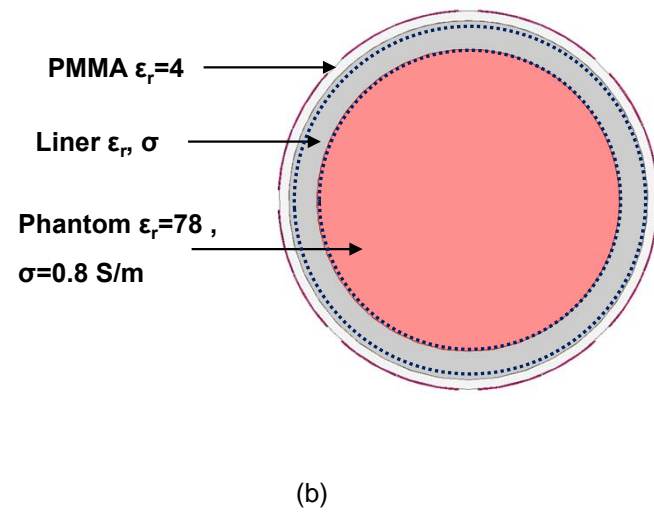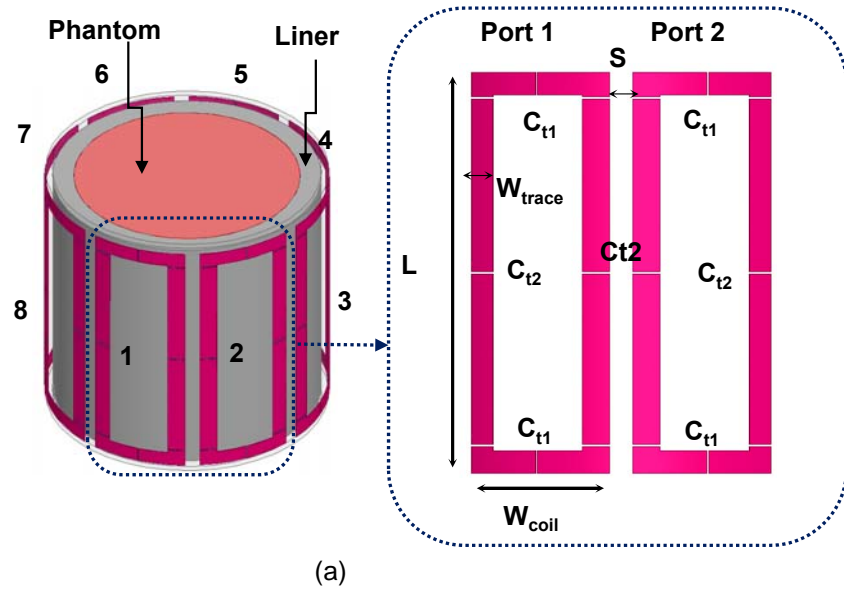**Figure 4 : Coil array connections for imaging measurements.**

Figure 5: B_1^+ field over a transverse slice in the middle of the phantom, and over a sagittal slice, with different liner permittivities (a, f) ε_r = 1 (air), (b, g) ε_r = 17.5, (c, h) ε_r = 35, (d, i) ε_r = 78, (e, j) ε_r = 150 with quadrature excitation. Dashed lines indicate the approximate locations of the transverse slices. Note the longitudinal asymmetry resulting from higher permittivities.

Figure 6: Local SAR in a transverse slice in middle of the phantom, and over a sagittal slice, with different liner permittivities: ε_r = 1 (a, f), ε_r = 17.5 (b, g), ε_r = 35 (c, h), ε_r = 78 (d, i), and ε_r = 150 (e, j) with quadrature excitation. Dashed lines indicate the approximate locations of the transverse slices. Note the longitudinal asymmetry resulting from higher permittivities.
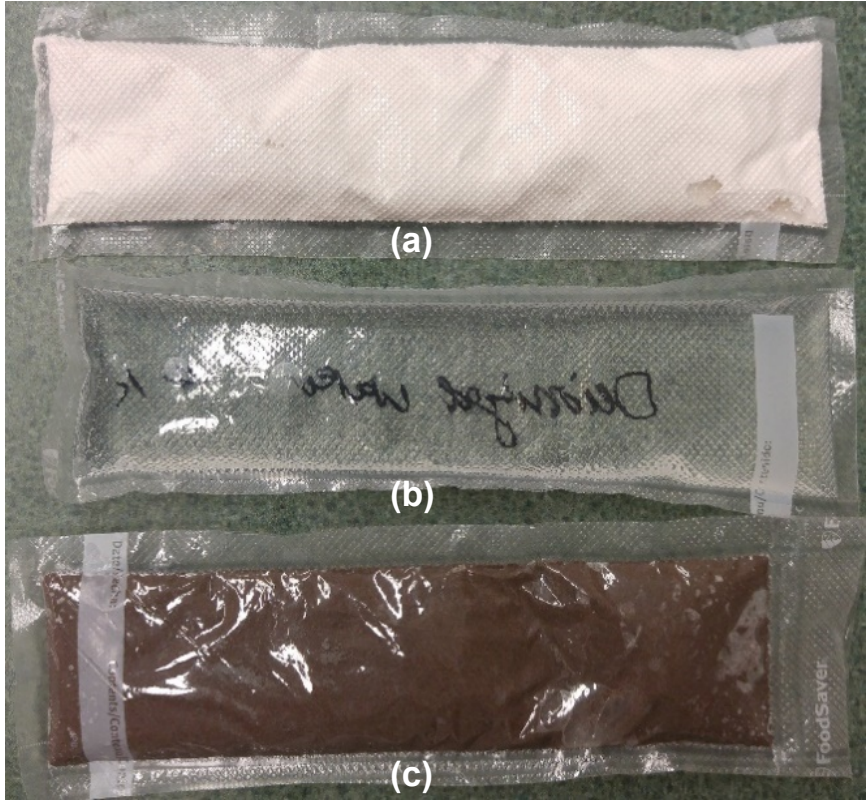
Figure 7: Comparison of the *S* matrix at 200 MHz after matching for different dielectric liners (ε_r = 1 (a), ε_r = 17.5 (b), ε_r = 35 (c), ε_r = 78 (d), and ε_r = 150 (e), respectively) in the presence of an ideal matching network at each port (S_{ii}=0). The impedance-matching alumina liner (b) results in minimal coupling (< -23 dB) overall.

Figure 8: Return loss ($|S_{11}|$) (a) measured on the bench, and corresponding simulation (b) for each liner permittivity. In both cases the optimal-permittivity liner gives the best performance.

Figure 9: Comparison of simulated fields (top row) from a single element to fields measured using the double-angle method (bottom row) with single-channel excitation. Liner permittivities are (a, e) $\varepsilon_r = 1$ (air), (b, f) $\varepsilon_r = 17.5$, (c, g) $\varepsilon_r = 78$, and (d, h) $\varepsilon_r = 150$. The driven coil is at the top of the image in all cases.

Phantom   Liner

6   5
7   4
8   3
1   2

Port 1   Port 2
S
C_{t1} C_{t1}
W_{trace}
L C_{t2} Ct2 C_{t2}
C_{t1} C_{t1}
W_{coil}

(a)

PMMA $\varepsilon_r=4$
Liner ε_r, σ
Phantom $\varepsilon_r=78$,
$\sigma=0.8$ S/m

(b)

(a)

(b)

(c)

50Ω

T/R 1 → Preamp 1

Transmit 1

T/R 2 → Preamp 2

50Ω

T/R 3 → Preamp 3

50Ω

T/R 4 → Preamp 4

50Ω loads

Coil array

1
8
2
7
3
6
4
5

(a)   (b)   (c)   (d)   (e)

(f)   (g)   (h)   (i)   (j)

0.1uT

0

(a)   (b)   (c)   (d)   (e)

5mW/kg

(f)   (g)   (h)   (i)   (j)

0

(a)   (b)   (c)   (d)   (e)

(a)

S$_{11}$ [dB]

frequency [MHz]

No pad
Matching pad
Water pad
BaTiO$_3$ pad

(b)

S$_{11}$ [dB]

frequency [MHz]

No pad
Matching pad
Water pad
BaTiO$_3$ pad